

# Lawrence Berkeley National Laboratory

LBL Publications

## Title

Electronic structure and spatial inhomogeneity of iron-based superconductor FeS\*\*Project supported by CAS-Shanghai Science Research Center, China (Grant No. CAS-SSRC-YH-2015-01), the National Key R&D Program of China (Grant No. 2017YFA0305400), t...

## Permalink

<https://escholarship.org/uc/item/2k68r7qd>

## Journal

Chinese Physics B, 29(4)

## ISSN

1674-1056

## Authors

Wang, Chengwei

Wang, Meixiao

Jiang, Juan

et al.

## Publication Date

2020-04-01

## DOI

10.1088/1674-1056/ab75d4

Peer reviewed

# Electronic Structure and Spatial Inhomogeneity of Iron-based Superconductor FeS

Chengwei Wang(王成玮)<sup>1,2,3,\*</sup>, Meixiao Wang(王美晓)<sup>2,\*</sup>, Juan Jiang(姜娟)<sup>2,4,\*</sup>,  
Haifeng Yang(杨海峰)<sup>2</sup>, Lexian Yang(杨乐仙)<sup>5</sup>, Wujun Shi(史武军)<sup>2</sup>, Xiaofang  
Lai(赖晓芳)<sup>6</sup>, Sung-Kwan Mo<sup>4</sup>, Alexei Barinov<sup>7</sup>, Binghai Yan(颜丙海)<sup>8</sup>, Zhi Liu(刘  
志)<sup>1,2</sup>, Fuqiang Huang(黄富强)<sup>6,9</sup>, Jinfeng Jia(贾金峰)<sup>10</sup>, Zhongkai Liu(柳仲楷)<sup>2,†</sup>  
and Yulin Chen(陈宇林)<sup>2, 5,11,‡</sup>

<sup>1</sup>State Key Laboratory of Functional Materials for Informatics, Shanghai  
Institute of Microsystem and Information Technology (SIMIT), Chinese  
Academy of Sciences, Shanghai 200050, P. R. China

<sup>2</sup>School of Physical Science and Technology, ShanghaiTech University, CAS-Shanghai  
Science Research Center, Shanghai 200031, P. R. China

<sup>3</sup>University of Chinese Academic of Sciences, Beijing 100049, P. R. China

<sup>4</sup>Advanced Light Source, Lawrence Berkeley National Laboratory, Berkeley, CA 94720, USA

<sup>5</sup>State Key Laboratory of Low Dimensional Quantum Physics, Department of Physics and  
Collaborative Innovation Center for Quantum Matter, Tsinghua University, Beijing 100084,  
P. R. China

<sup>6</sup>Beijing National Laboratory for Molecular Sciences and State Key Laboratory of Rare Earth  
Materials Chemistry and Applications, College of Chemistry and Molecular Engineering,  
Peking University, Beijing 100871, China

<sup>7</sup>Elettra-Sincrotrone Trieste ScPA, Trieste, Basovizza 34149, Italy

<sup>8</sup>Max Planck Institute for Chemical Physics of Solids, D-01187 Dresden, Germany

<sup>9</sup>State Key Laboratory of High Performance Ceramics and Superfine Microstructure,  
Shanghai Institute of Ceramics, Chinese Academy of Sciences, Shanghai 200050, China

<sup>10</sup>Key Laboratory of Artificial Structures and Quantum Control (Ministry of Education),  
Department of Physics and Astronomy, Shanghai Jiao Tong University, Shanghai 200240,  
China

<sup>11</sup>Physics Department, Oxford University, Oxford, OX1 3PU, UK

\*These authors contributed equally to this work.

†Corresponding author. E-mail: liuzhk@shanghaitech.edu.cn

‡Corresponding author. E-mail: yulin.chen@physics.ox.ac.uk

**ABSTRACT:** Iron-based superconductor family FeX (X = S, Se, Te) has been one of the  
research foci in physics and material science due to their record-breaking superconducting  
temperature (FeSe film) and rich physical phenomena. Recently, FeS, the least studied FeX  
compound (due to the difficulty in synthesising high quality macroscopic crystals) attracted

much attention because of its puzzling superconducting pairing symmetry. In this work, combining scanning tunnelling microscopy and angle resolved photoemission spectroscopy with sub-micron spatial resolution, we investigate the intrinsic electronic structures of superconducting FeS from individual single crystalline domains. Unlike FeTe or FeSe, FeS remains identical tetragonal structure from room temperature down to 5K, and the band structures observed can be well reproduced by our *ab-initio* calculations. Remarkably, mixed with the  $1 \times 1$  tetragonal metallic phase, we also observed the coexistence of  $\sqrt{5} \times \sqrt{5}$  reconstructed insulating phase in the crystal, which not only help explain the unusual properties of FeS, but also demonstrate the importance of using spatially resolved experimental tools in the study of this compound.

**Keywords:** angle-resolved photoemission with spatially resolution, scanning tunnelling microscopy, iron-based superconductor, electronic bandstructure

In the past few years, Fe-based superconductors (FeSCs) have been intensively studied due to their rich and unusual properties, such as multi-orbital band character<sup>[1]</sup>, close relation to magnetism<sup>[2]</sup>, intermediate correlation level<sup>[3]</sup> and complex pairing mechanism<sup>[4]</sup> – which make FeSCs rich yet intriguing system for the understanding of high temperature superconductivity<sup>[5-6]</sup>. Among FeSCs, the iron chalcogenide family compounds FeX ( $X = S, Se, Te$ ) have attracted enormous research interests recently due to their simple crystal structure, relatively strong correlation<sup>[3, 7]</sup> and the highest superconducting transition temperature ( $T_c$ ) among all FeSCs (thin film FeSe, see Ref. [8-10])

Despite the theoretical calculations that predicted similar electronic structures for all FeX compounds<sup>[11]</sup>, their physical properties show dramatic differences: while FeTe is non-superconducting and possesses an antiferromagnetic ground state below ~75 K with a large magnetic moment (~2.4  $\mu_B$ /Fe) and exhibits strong electron correlations<sup>[12-15]</sup>, FeSe superconducts ( $T_c \sim 8$  K for the bulk crystal<sup>[16]</sup> and ~65 K for the monolayer film on SrTiO<sub>3</sub><sup>[8-10]</sup>) and the superconductivity coexists with a nematic phase in the orthorhombic lattice ( $C_2$  symmetry) at low temperature which becomes tetragonal ( $C_4$  symmetry) above ~90 K<sup>[17-18]</sup>. FeS, the main focus of this work, also superconducts ( $T_c = 4.5$  K for the bulk crystal) with a tetragonal crystal structure, but without magnetic order<sup>[19-20]</sup> or phase transition to orthorhombic lattice. These differences from both FeTe and FeSe make it important to explore the electronic structure of FeS in order to understand the mechanism of superconductivity in FeX family, as well as the coexistence or competition of the superconducting order with other degrees of freedom (e.g. lattice and magnetism).

Unlike the numerous studies of FeTe and FeSe, up to date, the electronic structure of FeS still awaits experimental investigation, partially due to the difficulty in the synthesis of high quality macroscopic single crystalline samples - FeS was usually prepared by iron corrosion or co-precipitation methods and thus is very reactive toward oxygen and tends to transform into other iron sulphide phases<sup>[21-23]</sup>. Recently, high quality single crystals of FeS were successfully synthesized by mild hydrothermal reaction, and the bulk crystals superconduct at ~4.5K<sup>[19, 24]</sup>. Remarkably, recent thermal conductivity and specific heat measurements suggested a nodal superconducting gap structure in FeS<sup>[25]</sup>, making the mechanism of the superconductivity in FeX family elusive. Under this circumstance, the investigation on

electronic structures of FeS is urged, which, together with the comparison to those of FeTe and FeSe, will greatly help comprehend the unusual superconductivity in FeX family compounds.

Although the crystal quality of FeS has been significantly improved by hydrothermal reaction, typical single crystalline domain size is of tens of micrometers, less than the typical beamspot size (hundreds of micrometers) of most conventional ARPES setups, posing a great difficulty for the direct investigation of its electronic structure. In this letter, in addition to conventional ARPES, we further utilize the state-of-the-art spatially resolved ARPES with sub-micrometer resolution ( $\mu$ -ARPES) and scanning tunnelling microscopy (STM) to systematically investigate the electronic structure and spatial inhomogeneity of superconducting FeS single crystals. Our results clearly reveal the detailed topographic and electronic structure of FeS, showing clear  $C_4$  symmetry with multiple hole- and electron-pockets around the  $\bar{\Gamma}$  and  $\bar{M}$  points in its Fermi-surface, consistent with our *ab-initio* calculations. Interestingly, although the tetragonal phase and the associated electronic structures of FeS resemble those of FeTe and FeSe at high temperature; no tetragonal to orthorhombic phase transition was observed in FeS in a stark contrast to FeSe. This suggests a pure superconducting ground state in FeS and makes it a unique case among all the FeX compounds. Also remarkably, in addition to the metallic (tetragonal) phase, our  $\mu$ -ARPES and STM measurements further identified a coexisting  $\sqrt{5} \times \sqrt{5}$  reconstructed insulating phase in the crystal, which should be considered for the comprehensive understanding of the unusual properties in different measurements on macroscopic FeS

crystals (such as sample-to-sample variations in magnetism observed in the  $\mu$ SR measurement<sup>[26]</sup>).

The FeS crystals are prepared by hydrothermally extracting potassium atoms from parent material  $K_{0.8}Fe_{1.6}S_2$  synthesized in self-flux method<sup>[19]</sup> (and see Supplementary Information for details). Fig. 1(a) shows a tetragonal lattice structure of FeS composed of stacking edge-sharing  $FeS_4$ -tetrahedra with S atoms sitting above and below the Fe plane (P4/nmm space group), similar to other FeX in their tetragonal phase. The interaction between FeS layers is weak thus flat terrace structures could be observed in the synthesized FeS single crystals (see the SEM image in the inset of Fig. 1(b)). The tetragonal structure of FeS has been demonstrated by the X-ray diffraction pattern at room temperature (300K, Fig. 1(b)) and STM measurements at low temperature ( $\sim 5$  K) with atomic resolution (Fig. 1(c) and Supplementary Information). The fast-Fourier transformation (FFT) of the STM measurements in Fig. 1(c) clearly identified the lattice constant as  $a=b=3.681$  Å, confirming the tetragonal lattice structure of FeS at low temperature (Fig. 1(d)). In addition, STM topographic image in Fig. 1(c) shows multiple dumbbell shaped defects centered at the Fe atom sites (similar to the previous report in FeS<sup>[27]</sup> and FeSe<sup>[28-31]</sup>) that result from the substitution of Fe atoms by the excess S or alkali atoms (Na or K) during the crystal synthesis. The high quality of the FeS single crystal is also demonstrated by the sharp superconducting transition (Fig. 1(e)) and large superconducting volume (Fig. 1(f)) indicated by the resistivity and magnetic susceptibility measurements, respectively. From room temperature down to  $T_c$ , FeS behaves metallic and does not experience a structural phase transition (Fig. 1(b-f)), making it a unique case among the FeX family compounds.

We first investigate the general electronic structure of FeS by conventional ARPES (beamspot size is  $\sim 100 \mu\text{m}$ ). From the Fermi surface (FS) map (Fig. 2(a)(i)), we can identify pockets around the  $\bar{\Gamma}$  and  $\bar{M}$  points (the high symmetry points are defined in the 2-Fe BZ). From the dispersions along the high symmetry  $\bar{M} - \bar{\Gamma} - \bar{M}$  direction (Fig. 2(a)(ii)), it is clear that the pocket at  $\bar{\Gamma}$  is hole-like and those at  $\bar{M}$  are electron-like. The observed band structure can be well reproduced by our *ab-initio* calculations (Fig. 2(b)), where there are two hole/electron bands cross  $E_F$  around  $\bar{\Gamma}/\bar{M}$ , respectively. The two bands' crossing can be experimentally seen by polarizations measurements – as the total ARPES intensity depends on the transition matrix elements<sup>[32]</sup>, the photoemission intensity of the odd parity  $d_{xz}$  bands around  $\bar{\Gamma}$  is enhanced/suppressed with photon polarization perpendicular/parallel to the crystal mirror plane (Fig. 2(c)(i)); while the effect is opposite for the even parity  $d_{yz}$  bands (Fig. 2(c)(ii))<sup>[32-34]</sup>. We can thus use the linear horizontal (LH) and vertical (LV) polarization photons to selectively probe the  $d_{xz}$  and  $d_{yz}$  bands, respectively, as can be seen in Fig. 2(c)(i) and Fig. 2(c)(ii), respectively. In addition, the ARPES results also agree well with the STM measurements, as in Fig. 2(c)(iv), the integrated ARPES energy distribution curve (EDC) over the whole Brillouin zone (BZ) shows nice agreement with the  $dI/dV$  curve from our STM measurement (Fig. 2(c)(iv)), as both reflect the total density of state (DOS) from different bands of FeS.

The observed electronic structure of FeS shares broad similarities with other iron chalcogenides in their high-temperature tetragonal phase<sup>[35-37]</sup>, such as the number of hole bands/pockets around  $\bar{\Gamma}$  and electron bands/pockets around  $\bar{M}$ , and the orbital dependent enhancement of effective mass (the effective mass renormalization factor is  $\sim 2$  for the  $d_{xz}$  and

$d_{yz}$  band and  $\sim 3.5$  for the  $d_{xy}$  band; and the large renormalization of the  $d_{xy}$  band makes the bottom of the  $d_{xy}$  band sit above the  $d_{xz}$  hole band, similar to that in FeSe).

However, unlike FeSe or FeTe, the tetragonal crystal and electronic structures of FeS persist at low temperature ( $\sim 5\text{K}$ ); while at low temperature ( $T < \sim 90\text{K}$ ), FeSe shows two-fold orthorhombic symmetry<sup>[29, 35]</sup>, and FeTe enters the antiferromagnetic state with large magnetic moment (when  $T < \sim 75\text{K}$ ), leading to strong electron correlation and mode coupling (i.e., polarons<sup>[14]</sup>). Therefore, FeS represent the simplest and cleanest system among all FeX compounds, thus could serve as the best model system for the investigation of mechanism of the superconductivity in iron chalcogenides.

It is notable that in Fig. 2, the band dispersions and the FS map appear broad and while we were able to use different photon polarizations to enhance the bands with different symmetry, the geometry, such as the FS pockets shape, remains blurry without details. This is due to the fact that in the regular ARPES system, the photon beam spotsize ( $\sim 100\mu\text{m}$ ) is significantly larger than the typical domain size (up to  $\sim 30\mu\text{m}$ ) of the FeS crystals. Thus, the measurements represent the average of multiple domains which inevitably result in the relatively broader band structures as we observed in Fig.2.

To overcome this difficulty, we further performed the  $\mu$ -ARPES measurements (Fig. 3(a), the spot size is  $\sim 0.8\mu\text{m}$ , much smaller than the typical FeS domain size), and the results are assembled in Fig. 3 (more details can be found in the Supplementary Information). As can be seen in Fig. 3(b), the FeS crystal are composed of small single crystalline domains (brighter regions) ranging from a few micrometers up to tens of micrometers, which are intermediated

by the darker regions of either the insulating phases (as we will discuss below) or other impurities during the sample growth.

With the sub-micrometer photon beam spot, we were able to choose a large flat domain ( $\sim 35 \mu\text{m}$ , see Fig. 3(b)(iii)) for the  $\mu$ -ARPES measurements. Indeed, the results (Fig. 3(c)) shows clear improvement over the conventional ARPES results (Fig. 3(d)), and the detailed shape of the FS pockets is now discernible – even the different shape of the FS pockets at the  $\bar{\Gamma}$  points from different BZs (Fig. 3(c)(ii)) are now clearly seen: while the FS pocket near the 1<sup>st</sup>  $\bar{\Gamma}$  looks elliptical, the FS pocket at the 2<sup>nd</sup>  $\bar{\Gamma}$  has a cross-shape, and this difference becomes more apparent in the constant energy contours at higher binding energies (Fig. 3(c)(ii)). The different shapes of the FS pockets from different BZs can be explained by Fig. 3(e), where the orbital components of the FS pockets around the 1<sup>st</sup> and 2<sup>nd</sup>  $\bar{\Gamma}$  point (Fig. 3(e)) that can be observed by ARPES are different, similar to previous ARPES studies in  $\text{FeSe}_{1-x}\text{Te}_x$ <sup>[38]</sup> and other iron pnictides<sup>[39]</sup>.

To understand the nature of the intermediate phase (the darker region in Fig. 3(b)), we carried out STM topographic measurements. Remarkably, in addition to the tetragonal  $1 \times 1$  phase as we studied before (with lattice constant  $3.68 \text{ \AA}$ , see Fig. 4(b)(i-iii), area 3), we observed well-ordered  $\sqrt{5} \times \sqrt{5}$  reconstructed phase (with square unit cell and lattice constant of  $8.23 \text{ \AA}$ , see Fig. 4(b)(i,ii,iv), area 1, 2), similar to those observed in the FeSe film epitaxially grown on graphene<sup>[28]</sup>. The  $\sqrt{5} \times \sqrt{5}$  reconstruct areas in FeS are typically tens of nano-meters, and the dI/dV conductance curve (Fig. 4(c)) clearly shows that it's much more insulating than the tetragonal region, showing an asymmetric energy gap of  $100\sim 200\text{meV}$  (Fig. 4(c)).

This observation is in consistent with the ARPES measurements (e.g. in Fig. 3(b)) as the insulating  $\sqrt{5} \times \sqrt{5}$  domains naturally contribute less photocurrents than the metallic tetragonal regions, thus is one viable origin for the darker regions in the spatial map in Fig. 3(b) (other explanations to be explored include the residue and intermediate phases after the hydrothermal reaction). Also, this phase can further broaden the spectra of regular ARPES measurements in Fig. 2 and Fig. 3(d) due to the mixture of difference phases. The existence of the  $\sqrt{5} \times \sqrt{5}$  phase not only makes it necessary to use spatially resolved experimental techniques in the investigation of FeS, but also suggest that prudent analysis is needed in the interpretation of macroscopic measurements on bulk crystals (e.g. electric transport, magnetoelectric effect, and quantum oscillations, etc.).

In summary, with combined STM and ARPES measurement, our work reveals the electronic band structure of the yet unexplored FeS, showing overall agreement with the *ab-initio* calculations. The similarity of FeS bandstructures to other FeX compounds at their high temperature phase sets FeS an ideal and clean system to understand the mechanism of superconductivity in the iron chalcogenide family. Compare with the non-superconducting FeTe with antiferromagnetic ground state, FeS doesn't hold any magnetic order comparing to FeTe, indicating the magnetic order competes with superconductivity in FeSCs. In comparison with the superconducting FeSe, both the orthorhombic lattice distortion and the nematic order is absent in FeS, indicating the nematicity may enhances superconducting temperature. In terms of the electronic structure, FeS bears the similar electronic structure with FeSe and FeSe<sub>0.5</sub>Te<sub>0.5</sub> in the tetragonal phase, which both have several hole pockets at  $\Gamma$  and electron pockets at M, suggesting the inter-pocket electron-hole interaction is the main

pairing mechanism in these compounds. The band renormalization in FeS is 2~3 for the hole-like bands, similar to that in FeSe<sub>0.5</sub>Te<sub>0.5</sub>, indicating the intermediate to strong correlation level plays an important role in the superconductivity in FeSCs<sup>[35-37]</sup>. Further, the  $\mu$ -ARPES and STM has clearly demonstrated the coexistence of  $1 \times 1$  and  $\sqrt{5} \times \sqrt{5}$  phases, showing the complexity of the material. Such observation is in agreement with formation of the insulating  $\sqrt{5} \times \sqrt{5}$  phase in Se-rich FeSe multilayer films<sup>[28]</sup>, indicating they have the same origin. During the formation of the superstructure, the kinetic energy is reduced and the electronic correlation is enhanced, creating the insulating phase.

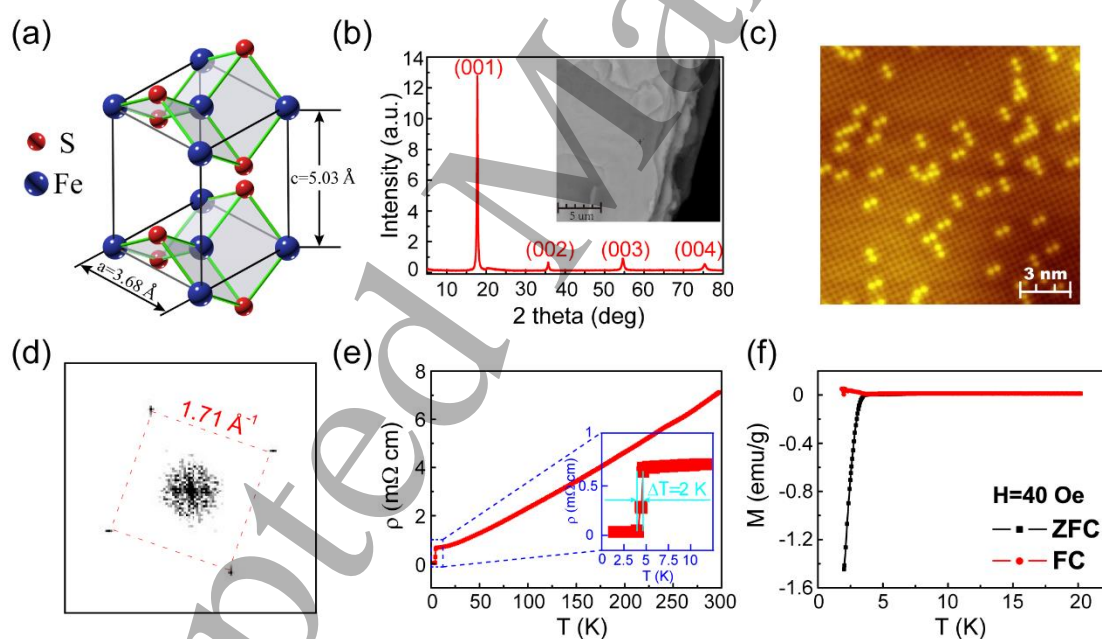


**Fig. 1 Physical Properties of hydrothermally synthesized FeS.** (a) Crystal structure of layered tetragonal FeS. (b) X-ray diffraction pattern and SEM image of FeS measured at room temperature. (c) STM topography image of FeS measured at  $\sim 5$ K. Dumb-bell-shape bright spots are defects from excess S or alkali metals from the synthesis process. (d) FFT of

(c) shows four spots forming a square. (e) Resistivity versus temperature curve. The inset shows the superconducting transition with  $\Delta T=2K$ . (f) Magnetic susceptibility versus temperature measured under a magnetic field of 40 Oe, in both zero-field-cooling (ZFC) and field-cooling (FC) processes.

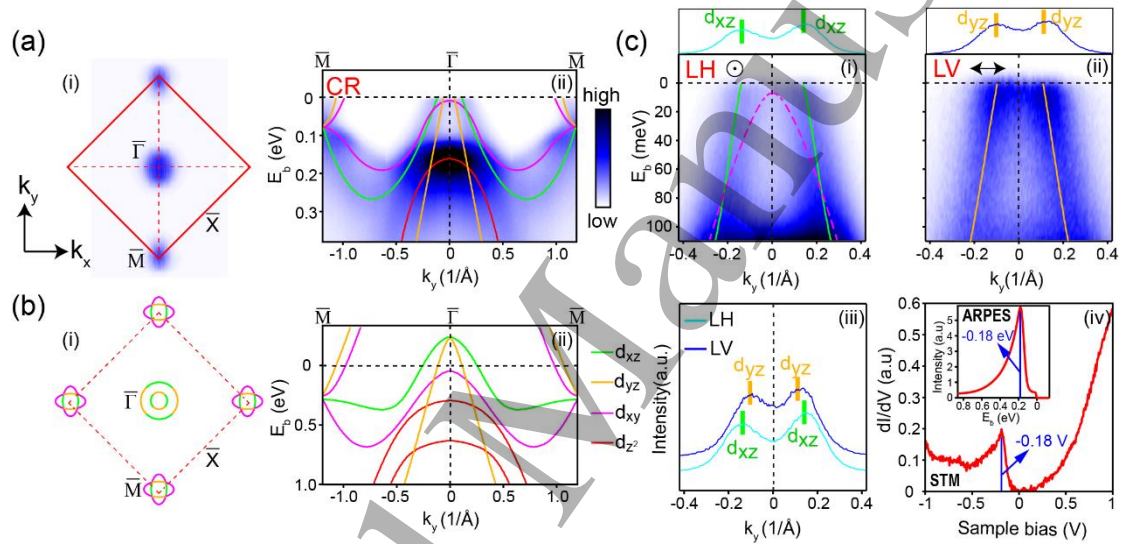


**Fig. 2 General Electronic Structure of FeS revealed by ARPES.** (a) Constant energy contour at the Fermi energy (i) and high symmetry  $\bar{\Gamma}$ - $\bar{M}$  cut (ii) measured with circularly right (CR) polarized light. The colored curves indicate the schematics of each band with different orbitals. (b) *Ab-initio* calculations of the Fermi surface (i) and high symmetry  $\bar{M}$  -  $\bar{\Gamma}$  -  $\bar{M}$  cut (ii) of FeS. Bands with different orbital characters are plotted with different colors. (c) High symmetry  $\bar{M}$  -  $\bar{\Gamma}$  -  $\bar{M}$  cut near the  $\bar{\Gamma}$  point measured with linear horizontal (LH)(i) and linear vertical (LV) (ii) polarized light. The direction of polarization with respect to the cut is labelled. Colored curves represent the bands with certain orbitals that are enhanced with the polarization. The magenta dotted curve indicates the  $d_{xy}$  orbital with very

weak intensity (similar to other FeX compounds, see Ref. [7]). The curves on top of (i) and (ii) are the momentum distribution curves (MDCs) at the Fermi energy. The peaks from fitting each MDC are indicated, showing the positions of each band. (iii) The stack plot of the two MDCs from (i) and (ii) showing the different positions of the  $k_F$  of the  $d_{xz}$  and  $d_{yz}$  bands. (iv) Comparison plot of the  $dI/dV$  curve obtained from STM and the integrated EDC (the inset figure) from (a)(ii). All ARPES data are measured with  $h\nu=25$  eV photons at  $T=8$  K sample temperature.

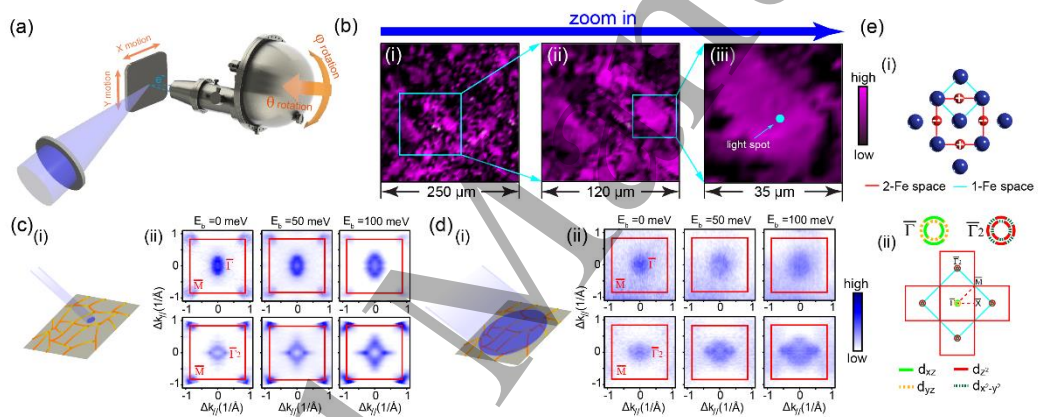


**Fig. 3 Electronic Structure of FeS studied by  $\mu$ -ARPES.** (a) Schematic diagram of the spatially resolved ARPES setup. (b) Spatial scan of FeS by  $\mu$ -ARPES from measuring the total photoemission intensity close to the Fermi level shows the domain size of single crystal FeS is around  $35 \mu\text{m} \times 35 \mu\text{m}$ . The position and size of the beam spot during the photoemission measurement is indicated by the blue circle in (iii). (c) Constant energy contours of FeS covering the first and second BZ at various binding energies measured by  $\mu$ -ARPES. (i) The schematic of the relative size of the beam spot and the FeS sample domain. (ii) The upper row plots the constant energy contours around the first  $\bar{\Gamma}$  at  $E_b = 0, 50$  and  $100$

meV, respectively. The lower row is the contour around the second  $\bar{\Gamma}$  at the same binding energies. Data are measured with  $h\nu = 74$  eV LH photons at  $T = 20$  K sample temperature. **(d)** Same as (c), the schematic of the relative beamspot size (i) and constant contour energy plots (ii) are from the conventional ARPES setup. Data are measured with  $h\nu = 180$  eV LH photons at  $T = 8$  K sample temperature, **(e)** (i) Illustration of the 1-Fe (blue square) and 2-Fe (red square) unit-cell in FeS. The S atoms above and below Fe plane are labelled by “+” and “-“, respectively. (ii) Illustration of the 1-Fe (blue square) and 2-Fe (red square) BZ and *ab-initio* calculation of the different orbital component of the bands near the  $\bar{\Gamma}$  point in the 1<sup>st</sup> and 2<sup>nd</sup> (2-Fe) BZ. Orbitals labelled with dotted curves indicate those suppressed by measurement beam using LH polarization (see Ref. [38]).

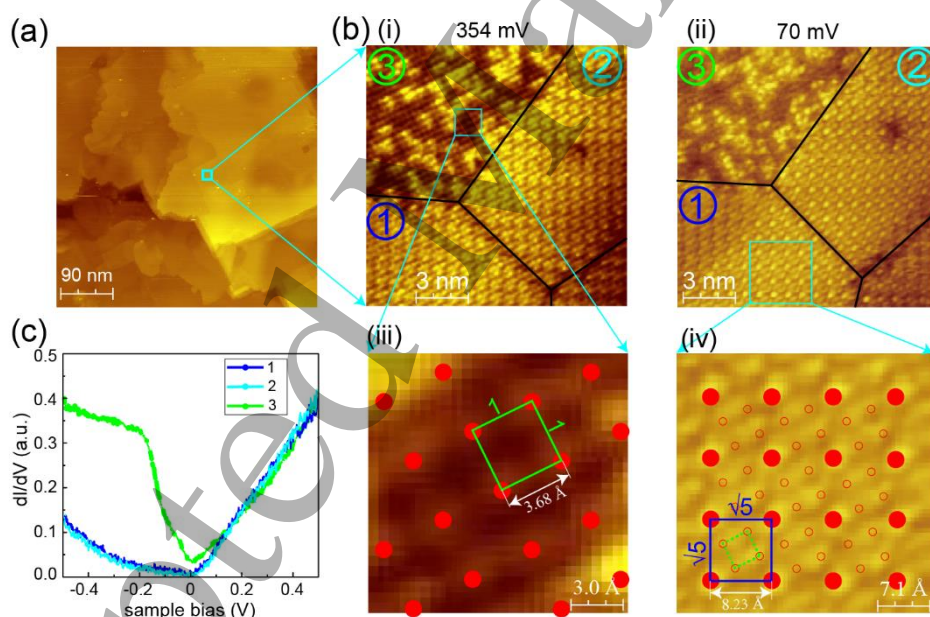


**Fig. 4 Spatial inhomogeneity in FeS.** **(a)** The topography image obtained by STM reveals flat terraces in FeS. **(b)** Zoomed-in topography scanned by STM at 354 mV (i) and 70 mV (ii) sample bias, respectively. Three coexisting regions are labelled. The details of the Region 3 in (i) and Region 1 in (ii) are plotted in (iii) and (iv), respectively. The superimposed red dots in (iii) and (iv) indicate sulphur atoms' positions on the surface in  $1 \times 1$  phase and  $\sqrt{5} \times \sqrt{5}$

phase, respectively. The smaller red empty circles in (iv) are the guidance for eyes showing the position of sulphur atoms in its corresponding  $1 \times 1$  phase. Colored squares indicate the smallest unit-cell found in each region. The size of each kind of unit-cell is labelled. (c) Typical dI/dV curves on three different regions.

### **Supporting Information**

Detailed introductions to: 1) Details of the synthesis of the FeS crystal. 2) Detailed information of STM experiment. 3) Detailed information about the  $\mu$ -ARPES experiment. 4) Resolving bands with different orbitals in FeS. 5)  $k_z$  dependence of the electronic structure of FeS.

### **Author Contributions:**

C.W.W., M.X.W. and J. J. equally contributed. Z.K.L. and Y.L.C. conceived and designed the experiments. M.X.W., C.W.W., J.J., H.F.Y. and Y.L.C performed ARPES measurements with the help from S.K.M. and A.B.; M.X.W. performed STM measurements. W.J.S. and B.H.Y. performed all DFT calculations. X.F.L. synthesized the FeS single crystals. M.X.W. C.C.W., Z.K.L. and Y.L.C. wrote the manuscript, with input from all authors.

### **Notes:**

The authors declare no competing financial interest.

## ACKNOWLEDGMENTS

This work is supported by grant from CAS-Shanghai Science Research Center, Grant No. CAS-SSRC-YH-2015-01. Z.K.L. acknowledges the support from the National Key R&D Program of China (Grant No. 2017YFA0305400) and National Natural Science Foundation of China (Grant No. 11674229). Y.L.C. acknowledges the support of the EPSRC Platform Grant (Grant No. EP/M020517/1) and Hefei Science Center CAS (2015HSC-UE013). Z.L. acknowledges the support from the National Natural Science Foundation of China (Grant No. 11227902) and Science and Technology Commission of Shanghai Municipality (Grant No. 14520722100). M.X.W. acknowledges the support from the National Natural Science Foundation of China (Grant No. 11604207). Advanced Light Source is operated by Office of Basic Energy Science of US DOE (contract DE-AC02-05CH11231). F.Q.H acknowledges the support from the Strategic Priority Research Program (B) of the Chinese Academy of Sciences: XDB04040200. We are also grateful for the beamtimes at the Spectromicroscopy beamline, Elettra synchrotron; Beamline 5-4, SSRL, SLAC National Laboratory; Beamline 10.0.1, ALS, LBNL; BL I05, DLS and BL13U, NSRL.

## References

- [1] Lu D H, Yi M, Mo S K, Erickson A S, Analytis J, Chu J H, Singh D J, Hussain Z, Geballe T H, Fisher I R, Shen Z X. 2008 *Nature* 455 81.
- [2] Cruz C D L.; Huang Q, Lynn J W, Li J, Li W R, Zarestky J L, Mook H A, Chen G F, Luo J L, Wang N L, Dai P. 2008 *Nature* 453 899.
- [3] Yin Z P, Haule K, Kotliar G. 2011 *Nature Materials* 10 932.
- [4] Chubukov A. 2012 *Annual Review of Condensed Matter Physics* 3 57.

- [5] Stewart G R. 2011 *Reviews of Modern Physics* 83 1589.
- [6] Paglione J, Greene R L. 2010 *Nature Physics* 6 645.
- [7] Yi M, Liu Z K, Zhang Y, Yu R, Zhu J X, Lee J J, Moore R G, Schmitt F T, Li W, Riggs S, Chu J H, Lv B, Hu J, Hashimoto M, Mo S K, Hussain Z, Mao Z Q, Chu C W, Fisher I R, Si Q, Shen Z X, Lu D H. 2015 *Nature Communications* 6 7777.
- [8] Wang Q Y, Li Z, Zhang W H, Zhang Z C, Zhang J S, Li W, Ding H, Ou Y B, Deng P, Chang K, Wen J, Song C L, He K, Jia J F, Ji S H, Wang Y Y, Wang L L, Chen X, Ma X C, Xue Q K. 2012 *Chinese Physics Letters* 29 037402.
- [9] Zhang W H, Sun Y, Zhang J S, Li F S, Guo M H, Zhao Y F, Zhang H M, Peng J P, Xing Y, Wang H C, Takeshi F, Akihiko H, Li Z, Ding H, Tang C J, Wang M, Wang Q Y, He K, Ji S H, Chen X, Wang J F, Xia Z C, Li L, Wang Y Y, Wang J, Wang L L, Chen M W, Xue Q K, Ma X C. 2014 *Chinese Physics Letters* 31 017401.
- [10] Ge J F, Liu Z L, Liu C, Gao C L, Qian D, Xue Q K, Liu Y, Jia J F. 2015 *Nature Materials* 14 285.
- [11] Subedi A, Zhang L, Singh D J, Du M H. 2008 *Physical Review B* 78 134514.
- [12] Ma F, Ji W, Hu J, Lu Z Y, Xiang T. 2009 *Physical Review Letters* 102 177003.
- [13] Jiang J, He C, Zhang Y, Xu M, Ge Q Q, Ye Z R, Chen F, Xie B P, Feng D L. 2013 *Physical Review B* 88 115130.
- [14] Liu Z K, He R H, Lu D H, Yi M, Chen Y L, Hashimoto, M, Moore R G, Mo S K, Nowadnick E A, Hu J, Liu T J, Mao Z Q, Devereaux T P, Hussain Z, Shen Z X. 2013 *Physical Review Letters* 110 037003.

- [15] Bao W, Qiu Y, Huang Q, Green M A, Zajdel P, Fitzsimmons M R, Zhernenkov M, Chang S, Fang M, Qian B, Vehstedt E K, Yang J, Pham H M, Spinu L, Mao Z Q. 2009 *Physical Review Letters* 102 247001.
- [16] Hsu F C, Luo J Y, Yeh K W, Chen T K, Huang T W, Wu P M, Lee Y C, Huang Y L, Chu Y Y, Yan D C, Wu M K. 2008 *Proceedings of the National Academy of Sciences* 105 14262.
- [17] McQueen T M, Williams A J, Stephens P W, Tao J, Zhu Y, Ksenofontov V, Casper F, Felser C, Cava R J. 2009 *Physical Review Letters* 103 057002.
- [18] Margadonna S, Takabayashi Y, McDonald M T, Kasperkiewicz K, Mizuguchi Y, Takano Y, Fitch A N, Suard E, Prassides K. 2008 *Chemical Communications* 43 5607.
- [19] Lai X F, Zhang H, Wang Y Q, Wang X, Zhang X, Lin J H, Huang F Q. 2015 *Journal of the American Chemical Society* 137 10148.
- [20] Lin H, Li Y, Deng Q, Xing J, Liu J, Zhu X, Yang H, Wen H H. 2016 *Physical Review B* 93 144505.
- [21] Boyd W C, Matsubara S. 1962 *Science* 137 669.
- [22] Denholme S J, Demura S, Okazaki H, Hara H, Deguchi K, Fujioka M, Ozaki T, Yamaguchi T, Takeya H, Takano Y. 2014 *Materials Chemistry and Physics* 147 50.
- [23] Denholme S J, Okazaki H, Demura S, Deguchi K, Fujioka M, Yamaguchi T, Takeya H, ElMassalami M, Fujiwara H, Wakita T, Yokoya T, Takano Y. 2014 *Science and Technology of Advanced Materials* 15 055007.
- [24] Pachmayr U, Fehn N, Johrendt D. 2016 *Chemical Communications* 52 194.

- [25] Xing J, Lin H, Li Y, Li S, Zhu X, Yang H, Wen H H. 2016 *Physical Review B* 93 104520.
- [26] Kirschner F K K, Lang F, Topping C V, Baker P J, Pratt F L, Wright S E, Woodruff D N, Clarke S J, Blundell S J. 2016 *Physical Review B* 94 134509.
- [27] Yang X, Du Z, Du G, Gu Q, Lin H, Fang D, Yang H, Zhu X, Wen H H. 2016 *Physical Review B* 94 024521.
- [28] Song C L, Wang Y L, Jiang Y P, Li Z, Wang L, He K, Chen X, Ma X C, Xue Q K. 2011 *Physical Review B* 84 020503.
- [29] Song C L, Wang Y L, Jiang Y P, Wang L, He K, Chen X, Hoffman J E, Ma X C, Xue Q K. 2012 *Physical Review Letters* 109 137004.
- [30] Song C L, Wang Y L, Cheng P, Jiang Y P, Li W, Zhang T, Li Z, He K, Wang L, Jia J F, Hung H H, Wu C, Ma X, Chen X, Xue Q K. 2011 *Science* 332 1410.
- [31] Watashige T, Tsutsumi Y, Hanaguri T, Kohsaka Y, Kasahara S, Furusaki A, Sigrist M, Meingast C, Wolf T, Löhneysen H V, Shibauchi T, Matsuda Y. 2015 *Physical Review X* 5 031022.
- [32] Wang X P, Richard P, Huang Y B, Miao H, Cevey L, Xu N, Sun Y J, Qian T, Xu Y M, Shi M, Hu J P, Dai X, Ding H. 2012 *Physical Review B* 85 214518.
- [33] Yi M, Lu D, Chu J H, Analytis J G, Sorini A P, Kemper A F, Moritz B, Mo S K, Moore R G, Hashimoto M, Lee W S, Hussain Z, Devereaux T P, Fisher I R, Shen Z X. 2011 *Proceedings of the National Academy of Sciences* 108 6878.

- [34] Chen F, Zhou B, Zhang Y, Wei J, Ou H W, Zhao J F, He C, Ge Q Q, Arita M, Shimada K, Namatame H, Taniguchi M, Lu Z Y, Hu J, Cui X Y, Feng D L. 2010 *Physical Review B* 81 014526.
- [35] Watson M D, Kim T K, Haghhighirad A A, Davies N R, McCollam A, Narayanan A, Blake S F, Chen Y L, Ghannadzadeh S, Schofield A J, Hoesch M, Meingast C, Wolf T, Coldea A I. 2015 *Physical Review B* 91 155106.
- [36] Watson M D, Kim T K, Haghhighirad A A, Blake S F, Davies N R, Hoesch M, Wolf T, Coldea A I. 2015 *Physical Review B* 92 121108.
- [37] Liu Z K, Yi M, Zhang Y, Hu J, Yu R, Zhu J X, He R H, Chen Y L, Hashimoto M, Moore R G, Mo S K, Hussain Z, Si Q, Mao Z Q, Lu D H, Shen Z X. 2015 *Physical Review B* 92 235138.
- [38] Moreschini L, Lin P H, Lin C H, Ku W, Innocenti D, Chang Y J, Walter A L, Kim K S, Brouet V, Yeh K W, Wu M K, Rotenberg E, Bostwick A, Grioni M. 2014 *Physical Review Letters* 112 087602.
- [39] Zabolotnyy V B, Inosov D S, Evtushinsky D V, Koitzsch A, Kordyuk A A, Sun G L, Park J T, Haug D, Hinkov V, Boris A V, Lin C T, Knupfer M, Yaresko A N, Buchner B, Varykhalov A, Follath R, Borisenko S V. 2009 *Nature* 457 569.